Energy Advances

PAPER

View Article Online
View Journal | View Issue

Check for updates

Cite this: *Energy Adv.*, 2024, 3, 861

A highly stable $Pr_2NiO_{4+\delta}$ oxygen electrode in electrolyte supported protonic ceramic electrolysis cells (PCECs) for hydrogen production with high faradaic efficiency

Leon Schley, [ab] Vaibhav Vibhu, [*a] Lucy Nohl, [a] Izaak C. Vinke, [a] L. G. J. (Bert) de Haart [a] and Rüdiger-A. Eichel [ab]

Received 8th November 2023,
Accepted 3rd March 2024

DOI: 10.1039/d3ya00542a

rsc.li/energy-advances

Protonic ceramic electrolysis cells are a promising technology for hydrogen production. However, parasitic electronic leakage in the ceramic electrolyte materials has detrimental effects on the faradaic efficiency and hence lowers overall efficiencies. Furthermore, the sluggish kinetics of the oxygen evolution reaction requires the development of efficient oxygen electrodes with high activity and durability at high steam contents. In this study, $BaCe_{0.7}Zr_{0.1}Y_{0.1}Yb_{0.1}O_{3-\delta}$ (BCZYYb7111) electrolyte supported single cells were fabricated and the electronic and ionic transport numbers in the electrolyte support were determined in dependence on the operating conditions. It was shown that the electronic leakage and thus the faradaic efficiency strongly depends on the operating temperature, steam partial pressure, oxygen partial pressure and current density. Optimal operating conditions were derived and faradaic efficiencies of ~95% were achieved at 600 °C and 20% H_2O. Furthermore, the comparison of $Pr_2NiO_{4+\delta}$ (PNO) and $Ba_{0.5}Sr_{0.5}Co_{0.8}Fe_{0.2}O_{3-\delta}$ (BSCF) as oxygen electrodes, showed higher current densities in electrolysis and fuel cell mode and lower polarization resistances (R_p) for PNO at intermediate temperatures between 600 to 700 °C. In the end, long-term measurements of the PNO/BCZYYb/Ni-BZY single cells in electrolysis mode showed stable behavior over 590 h.

Open Access Article. Published on 04 March 2024. Downloaded on 2/23/2026 10:43:05 PM.
This article is licensed under a Creative Commons Attribution 3.0 Unported Licence.

1. Introduction

Hydrogen production from steam electrolysis will play a key role in the near future to overcome the rapidly growing hydrogen demand in industry and to store the increasing amount of electric power from intermittent energy sources (*e.g.* wind and solar). While steam electrolysis technologies based on proton exchange membrane (PEM), alkaline (AE) and solid oxide electrolysis cell (SOEC) systems are already about to reach the pre-industrial scale, protonic ceramic electrolysis cells (PCECs) only exist on the laboratory scale so far. However, PCECs are sometimes referred to as next-generation steam electrolyzers, due to their high durability, high efficiency, and low-cost materials.[1,2]

The three main components in PCECs are a porous oxygen electrode (or steam splitting electrode), a dense proton conducting electrolyte and a porous fuel electrode. At the oxygen electrode, the oxygen evolution reaction (OER) takes place:

$$\text{OER: } H_2O \leftrightarrow 0.5O_2 + 2H^+ + 2e^- \quad (1)$$

where steam (H_2O) is consumed and oxygen (O_2), protons (H^+) and electrons (e^-) are evolved. While protons can travel through a dense protonic ceramic electrolyte, the electrons travel over an outer circuit towards the fuel electrode. There, the hydrogen evolution reaction (HER) takes place:

$$\text{HER: } 2H^+ + 2e^- \leftrightarrow H_2 \quad (2)$$

The HER shows that only hydrogen is involved in the reaction at the fuel electrode. This is a unique advantage of PCECs compared to SOECs, since no subsequent drying of hydrogen is necessary. Thus, overall system complexity and capital costs can be reduced.[2,3] Another advantage of PCECs are the promising intermediate operating temperatures (400–700 °C). Compared to the high operating temperatures (700–900 °C) of SOECs, the intermediate temperatures could facilitate smaller degradation rates and the use of more cost-effective materials on stack level (*e.g.* stack interconnectors) and balance-of-plant level (*e.g.* piping). Furthermore, smaller heat exchangers would be required in PCEC plants, which further could reduce investment costs.[2,4] Simultaneously, the intermediate temperatures offer more favorable thermodynamics and enhanced kinetics

[a] *Institute of Energy and Climate Research, Fundamental Electrochemistry (IEK-9), Forschungszentrum Jülich GmbH, 52425 Jülich, Germany. E-mail: v.vibhu@fz-juelich.de*
[b] *Institute of Physical Chemistry, RWTH Aachen University, 52074 Aachen, Germany*

© 2024 The Author(s). Published by the Royal Society of Chemistry

Open Access Article. Published on 04 March 2024. Downloaded on 2/23/2026 10:43:05 PM. This article is licensed under a Creative Commons Attribution 3.0 Unported Licence.

compared to the low temperature range (<100 °C) of PEM and alkaline electrolysis technologies. Thus, costly noble metal catalysts such as Ir or Pt are not required in PCECs.[5]

Typically, in PCECs Y-doped $BaCeO_3$, $BaZrO_3$ or $BaCeO_3$–$BaZrO_3$ solid solutions are used as electrolyte materials.[6] Here, ceria-rich electrolyte materials favor high proton conductivity, due to the high basicity/low electronegativity of ceria. However, in steam containing atmospheres or acidic gases like CO_2, high ceria contents facilitate the decomposition of $BaCeO_3$ into $BaCO_3$ and CeO_2 or $Ba(OH)_2$.[1,6] On the contrary, zirconia-rich electrolyte materials are more stable at high steam partial pressures but suffer from low sinterability.[1] Thus, high sintering temperatures are required for zirconia-rich electrolytes. This results in a trade-off between high proton conductivity and better sinterability of ceria rich electrolyte materials and higher stability of zirconia rich electrolyte materials.[1] In 2009, it was shown that $BaCeO_3$–$BaZrO_3$ solid solutions can be stabilized by Y and Yb co-doping, allowing high ceria contents with high proton conductivity and sufficient stability against H_2O and CO_2.[7] Within the tested compositions of $BaCe_{0.7}Zr_{0.1}Y_{0.2-x}Yb_xO_{3-\delta}$ (x = 0–0.2) a peak conductivity was obtained for $BaCe_{0.7}Zr_{0.1}Y_1Yb_1O_{3-\delta}$ (BCZYYb7111). Nowadays, the proposed composition of BCZYYb7111 is one of the most studied electrolyte materials and promising results were obtained in PCFC and PCEC applications.[7–13] However, in recent studies severe concerns about the chemical stability of BCZYYb7111 in H_2O or CO_2 rich atmospheres were raised.[14–17] Higher zirconium contents (>30–40 mol% of zirconium) were proposed to be necessary to achieve sufficient stability under these conditions. $BaCe_{0.4}Zr_{0.4}Y_{0.1}Yb_{0.1}O_{3-\delta}$ (BCZYYb4411)[15,18–20] or $BaCe_{0.5}Zr_{0.3}Y_{0.1}Yb_{0.1}O_{3-\delta}$ (BCZYYb5311)[21] could be more promising candidates, due to their higher stability compared to BCZYYb7111. However, the higher zirconium contents also leads to a decreased proton conductivity resulting in reduced performance of PCECs.[21] A direct comparison of the different electrolyte compositions in real fuel cell or electrolysis applications is scarce and would be highly valuable for the development of effective proton conducting cells.

Protonic conducting ceramics are often mixed ionic electronic conductors (MIECs) and possess ionic and electronic conductivity. In PCECs, the partial electronic conductivity of the electrolyte leads to parasitic electronic leakage and lowers the faradaic efficiency.[10] The electronic conductivity can be mainly attributed to p-type electronic conductivity near the oxidizing atmosphere of the oxygen electrode and n-type electronic conductivity near the reducing atmosphere of the hydrogen electrode.[22–24] Especially, p-type electronic conductivity becomes crucial under electrolysis mode operation, where the concentration profile of electronic charge carriers is dominated by the anodic overpotentials of the oxygen electrode.[10] To overcome this issue electrolyte materials with low electronic conductivity need to be developed.[10] Furthermore, the operating conditions (steam partial pressure, oxygen partial pressure, temperature and current density) can be tailored to increase the faradaic efficiencies.[25–28] In general, high steam partial pressures, low oxygen partial pressures and low temperatures tend to decrease the concentration of electronic holes and to increase the concentration of protonic defects resulting in increased faradaic efficiencies.[25–28] Regarding the effect of current density on the faradaic efficiency some contradictory results were published. Some studies report on decreasing faradaic efficiencies with increasing current density, since the increasing anodic overpotentials tend to increase the formation of electronic holes in the electrolyte, resulting in increased p-type conductivity and low faradaic efficiencies.[19,29–31] Other studies report on an increasing faradaic efficiency with increasing current density, where a net hydrogen loss close to the open circuit voltage (OCV) is assumed resulting in a minimum faradaic efficiency at OCV. With increasing hydrogen production at higher current densities, the hydrogen loss is mitigated, resulting in increasing faradaic efficiencies with increasing current densities.[10,18] In addition to electrolyte composition and operating conditions, also the electrolyte thickness could influence the ionic and electronic transport properties in the electrolyte. Here, increasing the electrolyte thickness could mitigate the influence of anodic overpotentials on the formation of electronic holes in the electrolyte resulting in increased faradaic efficiencies.[25,32] However, only a few studies report on the effect of electrolyte thickness on faradaic efficiency and further evaluation is necessary.

Another major challenge in PCECs is the development of effective oxygen electrode materials.[11] Since, protons (H^+), electrons (e^-) and steam (H_2O) are involved in the oxygen evolution reaction, the oxygen electrode should possess high conductivity towards these two charge carriers (H^+, e^-) and allow for the gas phase transport of steam and oxygen. Furthermore, active sites in the oxygen electrode material are required to catalyze the reaction.[2,11,33] Until now, a few promising oxygen electrode materials were identified, which can be classified into simple perovskites ($ABO_{3-\delta}$), double perovskites ($AA'B_2O_{6-\delta}$) and Ruddlesden–Popper phases ($A_2BO_{4+\delta}$). Promising results were obtained with simple perovskites such as $Ba_{0.5}Sr_{0.5}Co_{0.8}Fe_{0.2}O_{3-\delta}$ (BSCF),[34,35] $BaCo_{0.4}Fe_{0.4}Zr_{0.1}Y_{0.1}O_{3-\delta}$ (BCFZY)[10,36] or $PrNi_{0.5}Co_{0.5}O_{3-\delta}$ (PNC)[20,37] and double perovskites such as $PrBa_{0.5}Sr_{0.5}Co_{1.5}Fe_{0.5}O_{6-\delta}$ (PBSCF)[15,18,38] or $Ba_{0.5}Gd_{0.8}La_{0.7}Co_2O_{6-\delta}$ (BGLC),[29,31] which show low polarization resistances and high activity towards the OER. Lately, Ruddlesden–Popper nickelates such as $Pr_2NiO_{4+\delta}$ (PNO)[39,40] and derivatives[13,41] were shown to exhibit protonic and electronic conductivity and were proposed as effective oxygen electrode materials for protonic ceramic cells. The structure of $Pr_2NiO_{4+\delta}$ can be described as alternate layers of PrO rock-salt and NiO_6 octahedra layers.[42] The characteristic feature of these oxides is that they can accommodate interstitial oxygens in the PrO layers leading to a mixed valence of nickel (Ni^{2+}/Ni^{3+}) and hence to a mixed conductivity. At intermediate temperatures (500–600 °C), PNO shows even better electrochemical performance than the promising oxygen electrode BSCF.[40,43]

Finally, high durability of cell components is required, to facilitate the commercialization of PCEC systems. Especially, phase instability of electrolyte and oxygen electrodes at high steam partial pressures could lead to accelerated cell

© 2024 The Author(s). Published by the Royal Society of Chemistry

Open Access Article. Published on 04 March 2024. Downloaded on 2/23/2026 10:43:05 PM. This article is licensed under a Creative Commons Attribution 3.0 Unported Licence.

degradation.[9] Furthermore, thermo-mechanical incompatibility between electrolyte and oxygen electrode materials could lead to stress formation during temperature variations and subsequently to delamination at the electrolyte/electrode interface.[9] Here, similar thermal expansion coefficients (TECs) of the cell components could prevent severe cell degradation. In this respect, PNO could be more suited compared to other electrode materials since the TEC of PNO ($\sim 13.2 \times 10^{-6}$) is close to the TEC of BCZY electrolytes (8–12 $\times 10^{-6}$).[9,11] In contrast, BSCF, PBSCF and BCFZY exhibit relatively higher TECs of 23.2 $\times 10^{-6}$ K^{-1}, 23.7 $\times 10^{-6}$ K^{-1} and 21.6 $\times 10^{-6}$ K^{-1}. However, long-term measurements are scarce and only a few studies report on the durability of PCECs over 500 h.[10,18] Promising results were obtained with BCFZY as oxygen electrode, which showed stable electrolysis mode operation at a current density of 1.385 A cm^{-2} over 1200 h at 550 °C and 10% steam partial pressure with a small degradation rate of only 30 mV per 1000 hours.[10] However, a slight phase instability of BCFZY and an increase of the polarization resistance after long-term operation was observed, which became more severe at higher steam partial pressures.[10] Also, the promising oxygen electrode BGLC showed a significant degradation after subjecting it for 65 h to 1.5 bar H_2O and 600 °C.[31] The degradation of BGLC was attributed to secondary phase formation identified as $BaCoO_3$.[31]

In this study, three of the main challenges in PCECs were investigated. Firstly, electrolyte supported single cells with PNO or BSCF oxygen electrodes were fabricated and the electrochemical performance of PNO and BSCF was compared in electrolysis and fuel cell mode. Secondly, the electronic leakage in the BCZYYb7111 electrolyte material was determined in dependence of the operating conditions (temperature, steam partial pressure and current density). Thirdly, long-term measurements with PNO/BCZYYb/Ni-BZY single cells were performed in electrolysis mode to determine the durability of the cell components.

2. Experimental

2.1. Cell fabrication

Precursor powders. $BaCe_{0.7}Zr_{0.1}Y_{0.1}Yb_{0.1}O_{3-\delta}$ (BCZYYb7111) electrolyte powders were prepared by mixing proper amounts of $BaCO_3$ (AlfaAesar, 99.95%), CeO_2 (Aldich, 99.9%), ZrO_2 (AlfaAesar, 99.7%), Y_2O_3 (Aldich, 99.99%), Yb_2O_3 (Thermo Scientific, 99.9%) with the addition of 1 wt% NiO (AlfaAesar, 99.9%) as sintering aid. This raw precursor mixture was ball-milled in isopropanol with 3 mm YSZ balls for 48 h. After ball-milling, the powder was dried in air on a hot plate at 90 °C. Subsequently, a pure BCZYYb7111 phase powder was synthesized via reactive sintering at 1400 °C for 8 h. The $Pr_2NiO_{4+\delta}$ (PNO) powder was prepared using a solid state synthesis route as discussed elsewhere.[44] Commercial $Ba_{0.5}Sr_{0.5}Co_{0.8}Fe_{0.2}O_{3-\delta}$ (BSCF) (Cerpotech, >99%) and commercial NiO–$BaZr_{0.9}Y_{0.1}O_{3-\delta}$ (Ni-BZY) (Cerpotech, 60–40 vol%) were used.

Fabrication of electrolyte supports and electrode layers. BCZYYb7111 pellets were prepared by dry-pressing 2–3 g of the electrolyte precursor powder in its green state under 50 MPa for 1 min in a circular steel die set (∅ ~ 25 mm). The pressed pellets were sintered at 1400 °C for 8 h. During sintering the diameter of the pellets decreased to ~19 mm. Subsequently, the as-sintered pellets were polished from both sides to obtain a smooth surface. The electrolyte thickness was ~850 μm after polishing. The screen-printing pastes of the electrode materials *i.e.* Ni-BZY, PNO and BSCF were prepared by mixing the respective powder with α-terpineol and ethyl cellulose using a planetary vacuum mixer (THINKY Mixer ARV-310) and subsequently homogenized by roll-milling for 30 min, as described elsewhere.[45] The Ni-BZY fuel electrode was screen-printed (∅ ~ 12 mm) on one side of the electrolyte and sintered at 1400 °C for 2 h. After sintering the thickness of the fuel electrode was ~40 μm. Afterwards, the PNO or BSCF oxygen electrode was screen-printed (∅ ~ 10 mm) on the other side of the electrolyte and sintered at 1150 °C (PNO) or 1050 °C (BSCF) for 2 h.[39] After sintering the thickness of the oxygen electrodes were ~30 μm. Finally, thin current collecting layers of NiO and $LaNi_{0.7}Fe_{0.3}O_3$ (LNF) were screen-printed on the fuel electrode and oxygen electrode, respectively.[46,47]

2.2. XRD and microstructural analysis

The phase purity of as sintered BCZYYb7111 electrolyte powder was analyzed by X-ray diffraction (XRD) using a PANanalytical X'pert MPD diffractometer with Cu-Kα incident radiation. The single cell microstructure was analyzed with Quanta FEG 650 (FEI©) scanning electron microscope (SEM) equipped with an EDS detector at 20 kV.

2.3. Electrochemical characterization

The single cells were electrochemically characterized with a two-electrode (four-wire) NorECs Probostat (Norwegian Electro Cermacis®, NORECS, Oslo, Norway) setup. A gold current collector at the air side and a Pt–Ni current collector at the fuel side were used for electrode contacting. A gold ring was used for sealing. The respective gas flow was controlled by mass flow controllers (El-Flow®, Bronkhorst Nord, Kamen, Germany).

After mounting the single cell in the measurement set-up, it was heated up from room temperature to 900 °C for 2 h and cooled down to 700 °C with a heating and cooling rate of 1 °C min^{-1} using 9 Nl h^{-1} of N_2 at the fuel and 9 Nl h^{-1} of air at the oxygen electrode side. At 700 °C NiO at the fuel electrode was reduced to Ni by stepwise increasing the hydrogen flow rate from 1–9 Nl h^{-1} and lowering the nitrogen flow rate.[48]

After the reduction the first electrochemical measurements were performed in fuel cell mode with dry air at the oxygen electrode and dry hydrogen at the fuel electrode to check the quality of the cell mounting. The *iV* curves and impedance measurements were performed at 700, 675, 650, 625 and 600 °C. The *iV* curves were recorded using a scan rate of 10 mV s^{-1} starting from OCV to 0.4 V and back to OCV. Impedance measurements were recorded at OCV under potentiostatic control with a 20 mV ac amplitude, in a frequency range of 0.11 Hz to 110 kHz with 21 data points per frequency decade.

After operation in fuel cell mode, electrochemical measurements were performed in reversible mode with wet air (3, 10, 20

Open Access Article. Published on 04 March 2024. Downloaded on 2/23/2026 10:43:05 PM. This article is licensed under a Creative Commons Attribution 3.0 Unported Licence.

and 30% H_2O) at the oxygen electrode and dry hydrogen at the fuel electrode. The *iV* curves and impedance measurements were performed at 700, 675, 650, 625 and 600 °C at each steam partial pressure. The *iV* curves were recorded using a scan rate of 10 mV s^{-1} starting from OCV to 1.5 V to 0.4 V and back to OCV. Impedance measurements were recorded similarly to the fuel cell mode described above.

Long-term measurements in electrolysis mode were recorded galvanostatically by applying an electrolysis current density of −100 mA cm^{-2} and measuring the voltage for 590 h. The temperature was set to 700 °C and wet air (10% H_2O) was used at the oxygen electrode and dry hydrogen at the fuel electrode.

3. Results and discussion

3.1. Structural and microstructural analysis

Fig. 1(a) shows the X-ray diffractogram of as sintered BCZYYb7111 electrolyte powder, sintered at 1400 °C for 8 h. A pure BCZYYb7111 phase was obtained after sintering and no secondary phases can be observed. Fig. 1(b) shows the cross-section images of a fractured BCZYYb7111 electrolyte support sintered at 1400 for 8 h. The BCZYYb7111 electrolyte has a dense and gas tight structure with a large grain size of ≥7 μm. In other electrolyte materials with a higher Zr-content, for example, BZCY541, smaller grain sizes of only ∼2 μm were achieved.[29] This could be explained by the lower sinter-ability of Zr-rich electrolyte materials, leading to smaller grain sizes.

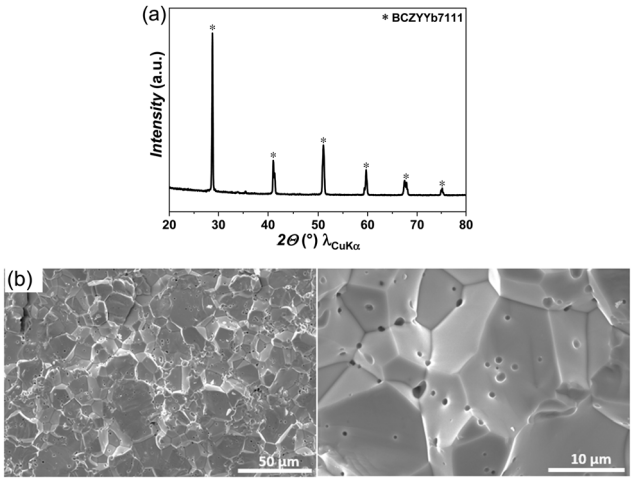

Fig. 1 (a) XRD pattern of as-sintered BCZYYb7111 electrolyte powder, and (b) cross-sectional SEM images of BCZYYb7111 electrolyte support, sintered at 1400 °C for 8 h.

3.2. Electrochemical characterization of single cells

3.2.1. Comparison of PNO and BSCF as oxygen electrode. To compare the electrochemical performance of PNO and BSCF oxygen electrodes, *iV* curves and impedance data of the single cells were recorded. Similar BCZYYb7111 electrolyte supports and Ni-BZY fuel electrodes were used. While the BCZYYb7111 electrolyte support was prepared by solid state reactive sintering (SSRS) in house, commercial Ni-BZY powder was used as fuel electrode just for the comparison of the cells. Fig. 2(a) shows the influence of PNO and BSCF oxygen electrodes on *iV* curves at 600 °C with wet air (10% H_2O) at the air side and dry hydrogen at the fuel side. Increased performance was obtained with PNO oxygen electrodes in both electrolysis and fuel cell mode. For instance, at 1.5 V electrolysis current densities of −75 mA cm^{-2} and −66 mA cm^{-2} were achieved with a PNO and a BSCF oxygen electrode, respectively. Fig. 2(b) shows the Nyquist-plots of the different single cells measured under OCV at 600 °C. Similar ohmic resistances of 4.82 and 4.79 Ω cm^2 were obtained, proving that the electrolytes of the different single cells were similar in terms of ion conductivity and thickness. Contrarily, the polarization resistances (R_p) increased from 1.25 Ω cm^2 for the cell with a PNO oxygen electrode to 2.61 Ω cm^2 for the cell with BSCF as oxygen electrode.

3.2.2. *iV* curves. Fig. 3(a) shows the *iV* curves of PNO/BCZYYb/Ni-BZY single cells at 600 °C and different steam partial pressures (0, 3, 10 and 20% H_2O) at the oxygen electrode. In electrolysis mode, the cell performance slightly increases with an increasing steam partial pressure, which can be mainly attributed to the decreasing OCV values at higher steam contents. For instance, at 1.5 V, electrolysis current densities of −71, −75 and −79 mA cm^{-2} were obtained at 600 °C for 3, 10 and 20% steam, respectively. These values are rather low compared to latest results from literature with fuel electrode supported cells, where electrolysis current densities of ∼1500 mA cm^{-2} at 1.5 V and 600 °C were achieved.[10] The lower performance of our electrolyte supported cells can be mainly attributed to the increased electrolyte thickness of 844 μm compared to an electrolyte thickness of ∼15 μm for fuel electrode supported cells.[10] However, compared to other electrolyte supported cells, our electrolyte supported cell shows rather good performance. For example, a low current density of ∼18 mA cm^{-2} was achieved with a 450 μm thick $BaCe_{0.9}Y_{0.1}O_{3-\delta}$ (BCY91) electrolyte at 1.5 V and 600 °C.[49] Similarly, a low electrolysis current density of ∼15 mA cm^{-2} was achieved with a 500 μm thick $BaCe_{0.2}Zr_{0.7}Y_{0.1}O_{3-\delta}$ (BZCY271) electrolyte at 1.5 V and 700 °C.[50]

In fuel cell mode, the cell performance decreases with increasing steam partial pressure at the oxygen electrode. Highest fuel cell performance was obtained with dry air. The decreasing performance in fuel cell mode with increasing steam pressures can be attributed to the lower OCV values and the impeded steam removal from the oxygen electrode at increased steam contents. Furthermore, the *iV* curves in Fig. 3 shows that PNO/BCZYYb/Ni-BZY single cells can be easily operated in fuel cell and electrolysis reversible mode without changing gas compositions or cell configuration. Fig. 3(b) shows the temperature dependency of the *iV* curves at 20% H_2O between 700 and 600 °C. An increase in current density with increasing temperature is observed. For instance, at 1.5 V electrolysis current densities of −79, −112 and −152 mA cm^{-2} were achieved at 600, 650 and 700 °C, respectively. Because of

© 2024 The Author(s). Published by the Royal Society of Chemistry

Open Access Article. Published on 04 March 2024. Downloaded on 2/23/2026 10:43:05 PM. This article is licensed under a Creative Commons Attribution 3.0 Unported Licence.

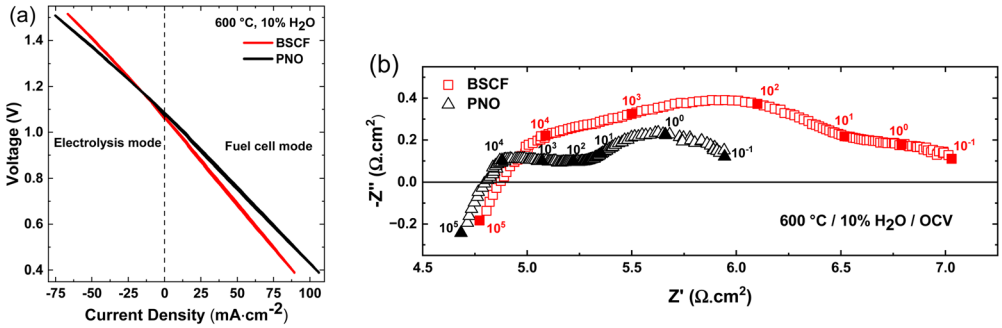

Fig. 2 Comparison of PNO and BSCF oxygen electrodes. (a) *iV* curves and (b) Nyquist plots of BCZYYb7111 electrolyte supported cells with PNO or BSCF as oxygen electrode. The temperature was set to 600 °C and wet air (10% H_2O) and dry hydrogen were used at the air and fuel side.

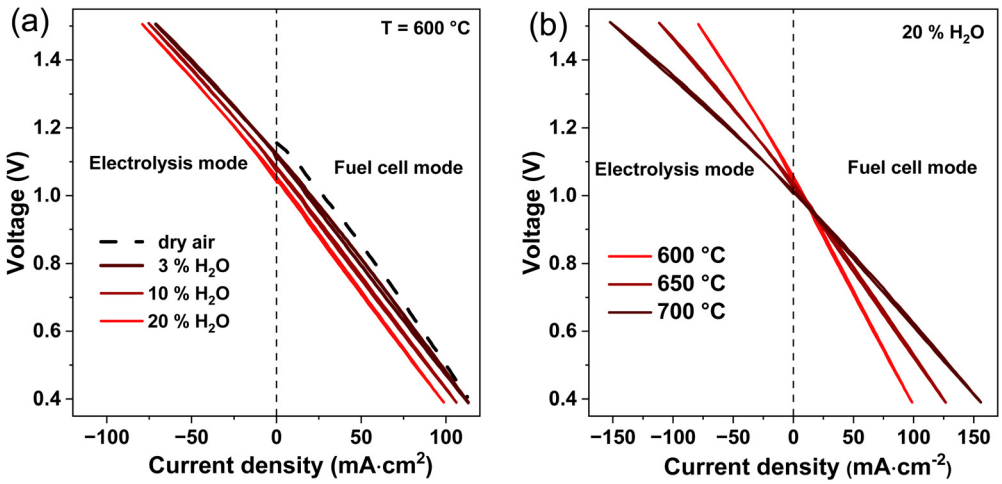

Fig. 3 *iV* curves of electrolyte supported PNO/BCZYYb/Ni-BZY single cells (a) at 600 °C and different steam partial pressures (0–30% H_2O in air) and (b) at 20% steam partial pressure in air and different temperatures (600–700 °C). In all measurements dry hydrogen was used at the fuel electrode.

the relatively low current densities and high ohmic resistances of our electrolyte supported cells compared to fuel electrode supported cells,[10] only temperatures above 600 °C were used in this study.

3.2.3. Impedance analysis. Impedance measurements of electrolyte supported PNO/BCZYYb/Ni-BZY single cells were performed to determine the ohmic (R_Ω) and polarization resistances (R_p). Fig. 4 shows the Nyquist plots at 650 °C and different steam partial pressures (0–30% H_2O in air) at the oxygen electrode. Both R_Ω and R_p increase with increasing steam partial pressures. R_Ω increases from 3.65 to 3.87 Ω cm^2 and R_p increases from 0.53 to 0.9 Ω cm^2 by increasing the steam partial pressure from 0 to 30%. The values for R_Ω are relatively high due to the relatively high electrolyte thickness of ~844 μm. However, assuming that R_Ω can be attributed to the electrolyte, a specific resistance of 4.6 mΩ cm^2 μm^{-1} can be calculated at 650 °C and 20% H_2O. Other electrolyte materials with increased Zr content, such as BZCY541[29] exhibit increased specific resistances of 30 mΩ cm^2 μm^{-1} (R_Ω = 0.36 Ω cm^2, thickness = 12 μm) in similar conditions. The comparably low specific ohmic resistance in our BCZYYb7111 support could be attributed to the higher proton conductivity of ceria rich electrolytes as well as the relatively large grain size of ~7 μm (Fig. 1) obtained in our electrolyte support.

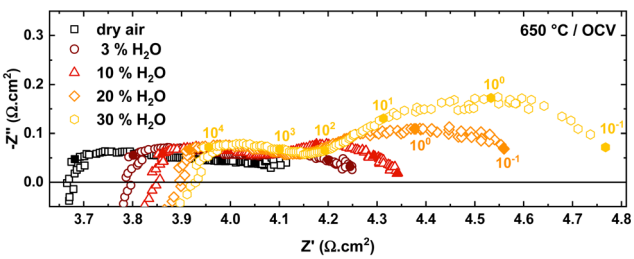

Fig. 4 Nyquist plots of PNO/BCZYYb/Ni-BZY single cells at 650 °C with wet air (0–30% H_2O) at the oxygen electrode and dry hydrogen at the fuel electrode.

The increasing ohmic and polarization resistance with increasing steam partial pressure could be explained by the decreasing electronic conductivity in the electrolyte and the oxygen electrode with higher steam partial pressures.[6,13] In simple perovskite materials, such as BCZYYb, protonic defects

Open Access Article. Published on 04 March 2024. Downloaded on 2/23/2026 10:43:05 PM.
This article is licensed under a Creative Commons Attribution 3.0 Unported Licence.

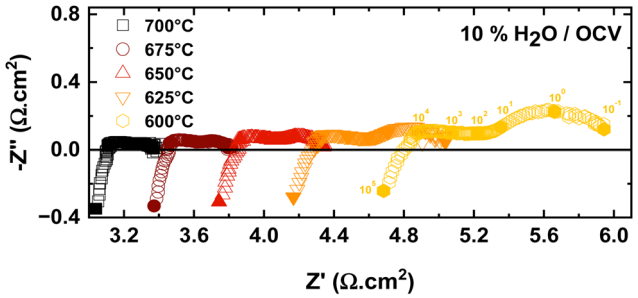

Fig. 5 Nyquist plots of PNO/BCZYYb/Ni-BZY single cells at 10% steam partial pressure at the oxygen electrode with varying temperatures.

are formed at the expense of oxygen vacancies or electron holes according to the following equations in Kröger–Vink notation:[6]

$$H_2O + V_O^{\bullet\bullet} + O_O^{\times} \leftrightarrow 2OH_O^{\bullet} \quad (3)$$

$$H_2O + 2O_O^{\times} + 2h^{\bullet} \leftrightarrow 2OH_O^{\bullet} + 0.5O_2 \quad (4)$$

where $V_O^{\bullet\bullet}$ are oxygen vacancies, $O_O^{\times}$ are oxygen ions on regular oxygen-sites, $h^{\bullet}$ are electron holes and $OH_O^{\bullet}$ are protonic defects.

Contrarily, in Ruddlesden–Popper phases, such as PNO, protonic defects are rather formed at interstitial sites.[13,39] Possible reaction mechanisms are as follows:[13,51]

$$H_2O + O_i'' \leftrightarrow 2OH_i' \quad (5)$$

$$H_2O + 2O_i'' + 2h^{\bullet} \leftrightarrow 2OH_i' + 0.5O_2 \quad (6)$$

where O_i'' are oxygen interstitials and OH_i' are hydroxide interstitials. As can be seen from eqn (4) and (6) high steam partial pressures lead to a decreasing concentration of electronic charge carriers ($h^{\bullet}$) in the electrolyte and oxygen electrode. Thus, a lower electronic conductivity in the electrolyte and electrode could be obtained at higher steam partial pressures leading to increased ohmic and polarization resistances.

The influence of operating temperature on the impedance data is shown in Fig. 5. Both R_Ω and R_p decrease with increasing temperature. While R_Ω decreases from 4.79 to 3.09 Ω cm^2, R_p decreases from 1.25 to 0.29 Ω cm^2, when the temperature is increased from 600 to 700 °C. The decreasing resistances with increasing temperature can be explained by the different temperature activated processes at the electrode/electrolyte interfaces and in the electrolyte.

In order to further distinguish between ionic and electronic resistances, an equivalent circuit shown in Fig. 6(a) was used, where R_e and R_i are the electronic and ionic resistances in the electrolyte, $R_{p,r}$ is the real polarization resistance of the electrode and V_N is the Nernst-potential.

At high frequencies, the capacitors are short circuited and the measured apparent ohmic resistance (R_Ω) from impedance analysis contains contributions of R_e and R_i, according to:[18,29]

$$R_\Omega = \frac{R_e R_i}{R_e + R_i} \quad (7)$$

At low frequencies the direct current resistance (R_{DC}) contains contributions of R_e, R_i and $R_{p,r}$, according to:[18,29]

$$R_{DC} = \frac{R_e(R_i + R_{p,r})}{R_e + R_i + R_{p,r}} \quad (8)$$

R_Ω and R_{DC} are measured values and can be determined with impedance analysis. In addition to eqn (7) and (8), a third equation for R_e can be derived from impedance data and OCV measurements. R_e can be expressed as:[18,29]

$$R_e = \frac{R_{DC}}{1 - \frac{V_{OCV}}{V_N}} \quad (9)$$

where V_{OCV} is the measured voltage at OCV and V_N is the calculated Nernst-potential. With these and the ionic transport number defined as:

$$t_i = \frac{R_e}{R_i + R_e} \quad (10)$$

R_i and $R_{p,r}$ can be expressed as functions of R_Ω, R_{DC} and t_i:[18,29]

$$R_i = \frac{R_\Omega}{t_i} \quad (11)$$

$$R_{p,r} = \frac{R_\Omega(R_{DC} - R_\Omega)}{t_i[t_i R_{DC} - (R_{DC} - R_\Omega)]} \quad (12)$$

In this study, the measured resistances R_Ω and R_{DC} as well as the calculated variables R_i, R_e, $R_{p,r}$ and t_i were determined at OCV, while the influence of the anodic overpotentials on the electronic and ionic resistances in the electrolyte was neglected. This is however a valid assumption, since the anodic

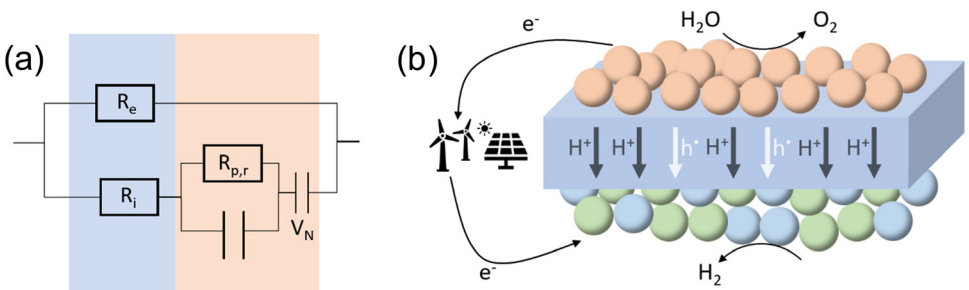

Fig. 6 Equivalent circuit for PCECs with mixed ionic electronic conducting electrolyte, (b) schematic illustration of proton ceramic cells (PCCs) in electrolysis mode.

© 2024 The Author(s). Published by the Royal Society of Chemistry

Open Access Article. Published on 04 March 2024. Downloaded on 2/23/2026 10:43:05 PM. This article is licensed under a Creative Commons Attribution 3.0 Unported Licence.

overpotentials only should have an influence in a distance of a few micrometers from the oxygen electrode, which can be neglected in our thick electrolyte support of ~850 μm. Eqn (11) and (12) show that the real ionic resistance (R_i) of the electrolyte and the real polarization resistance ($R_{p,r}$) of the electrode differs from the measured apparent ohmic (R_Ω) and polarization resistances (R_p). If the electrolyte exhibits pure ionic conductivity ($t_i = 1$), R_i and $R_{p,r}$ are equal to the measured R_Ω and R_p. Contrarily, if the electrolyte exhibits electronic conductivity ($t_i < 1$), R_i and $R_{p,r}$ will be larger than R_Ω and R_p. Thus, R_i and $R_{p,r}$ are sometimes underestimated with impedance analysis.

Fig. 7(a) and (b) show the Arrhenius plots for the measured resistances R_Ω, R_p, R_{DC} and calculated resistances R_i, $R_{p,r}$, R_e. The corresponding activation energies are also indicated. The activation energy for R_i (0.31 eV) is slightly lower than the activation energy for R_Ω (0.32 eV) and is in good agreement with the activation energy for proton conduction (0.3–0.5 eV) in protonic ceramic electrolytes.[1,6] Similarly, the activation energy for $R_{p,r}$ is slightly lower than for R_p and decreases from, 1.13 eV to 0.77 eV with increasing temperature. These values match well with data from literature, where also a PNO oxygen electrode was used.[39] Furthermore, Fig. 7(b) shows the electronic resistance of the electrolyte (R_e) in dependence of the temperature. With increasing temperature R_e decreases from 380 to 100 Ω cm^2. The decreasing R_e values indicate that p-type conductivity in the electrolyte increases with increasing temperatures. This can be explained by the exothermic character of the hydration reaction, see eqn (3).[6] While decreased temperatures favor the formation of protonic defects, increased temperatures favor the formation of electronic charge carriers and thus electronic conductivity. Furthermore, the activation energy for R_e (0.95 eV) is higher than for R_i (0.31 eV), which means that the electronic conductivity increases more rapidly with increasing temperature than the ionic conductivity in the electrolyte. Thus, high temperatures favor parasitic electronic leakage in PCECs.

Fig. 7(c) shows the ratio between apparent polarization resistance and real polarization resistance ($R_p/R_{p,r}$) and apparent ohmic resistance and real ionic resistance (R_Ω/R_i). The electronic conductivity in the electrolyte leads to a deviation between measured and real values. With increasing temperature from 600 to 700 °C, $R_p/R_{p,r}$ decreases from 0.97 to 0.94 and R_Ω/R_i decreases from 0.99 to 0.97. Both $R_p/R_{p,r}$ and R_Ω/R_i,

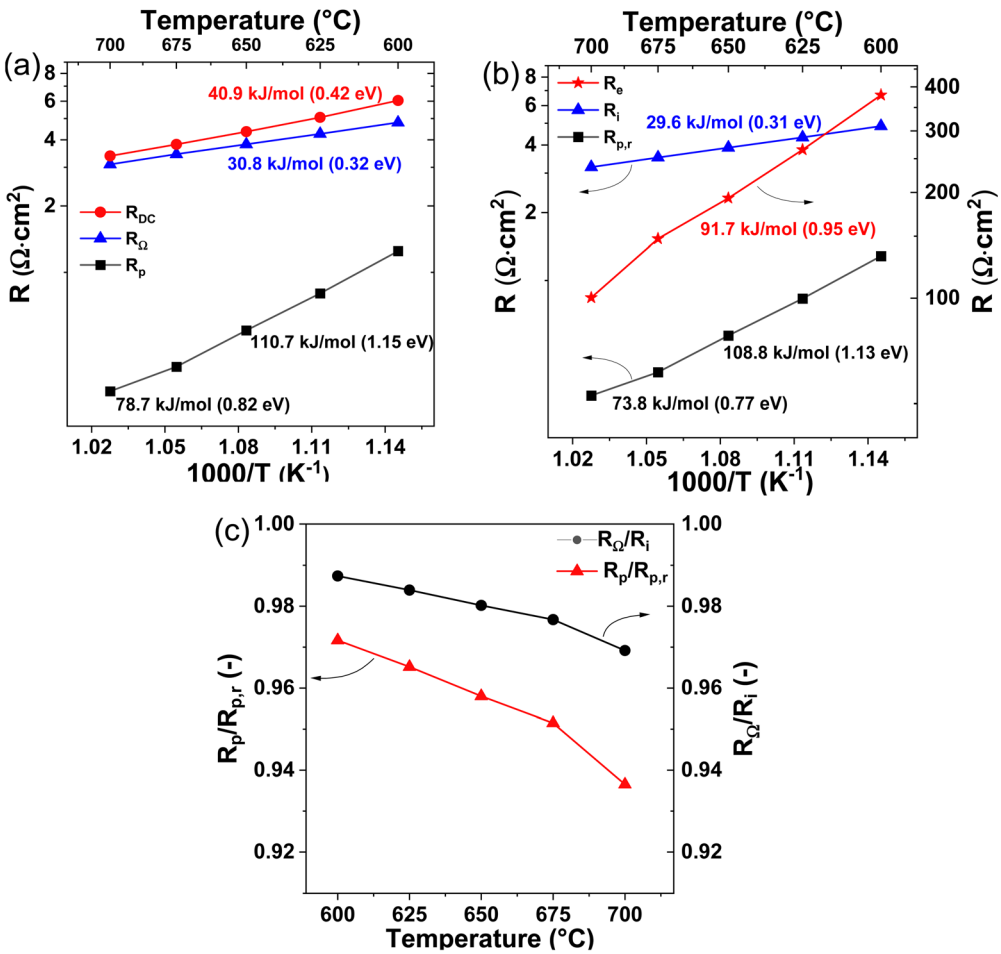

Fig. 7 Arrhenius plots of the (a) measured resistances R_{DC}, R_Ω and R_p and (b) calculated resistances R_e, R_i and $R_{p,r}$ of PNO/BCZYYb/Ni-BZY singles cells. (c) ratio of $R_p/R_{p,r}$ and R_Ω/R_i. Wet air (10% H_2O) was used at the oxygen electrode and dry hydrogen at the fuel electrode.

Open Access Article. Published on 04 March 2024. Downloaded on 2/23/2026 10:43:05 PM.
This article is licensed under a Creative Commons Attribution 3.0 Unported Licence.

exhibit values lower than 1, meaning that $R_{p,r}$ and R_i would be underestimated by using an equivalent circuit without a parallel resistor for the electronic conductivity of the electrolyte (R_e). The decreasing values for $R_p/R_{p,r}$ and R_Ω/R_i with temperature can be explained by the decreasing ionic transport numbers with increasing temperatures.

3.2.4. Faradaic efficiency. In PCECs the mixed ionic–electronic conductive behavior of $Ba(Ce,Zr)O_{3-\delta}$ leads to parasitic electronic leakage in the electrolyte. While in SOECs a pure ionic conductive electrolyte can be assumed with a faradaic efficiency of 100%, in PCECs faradaic efficiencies of 20–95% are reported depending on the electrolyte material, electrolyte thickness and operating conditions (steam partial pressure, temperature and current density).[25]

Determining the electronic leakage/faradaic efficiency in PCECs is challenging. One way to determine the faradaic efficiency is by measuring the hydrogen concentration at the cell outlet. However, since hydrogen is often also introduced at the cell inlet it is difficult to distinguish between produced hydrogen and introduced hydrogen, especially in the low current region. Therefore, in this study the faradaic efficiency is calculated from OCV measurements and impedance analysis.

The gap between measured open circuit voltage (V_{OCV}) and theoretical Nernst-potential (V_N) is an indicator for electronic leakage in PCCs. Fig. 8(a) and (b) show the measured voltages at OCV (V_{OCV}) and the theoretical Nernst-potentials (V_N) at 3% and 10% steam partial pressure on the oxygen electrode in dependence of the temperature. At 3% H_2O, the gap between V_{OCV} and V_N increases from 26.4 mV (2.3%) at 600 °C to 50.6 mV (4.7%) at 700 °C. The increasing deviation between V_{OCV} and V_N is a sign of increasing parasitic electronic leakage at higher temperatures. At 10% H_2O, the gap between V_{OCV} and V_N increases from 17.3 mV (1.6%) at 600 °C to 35.9 mV (3.5%) at 700 °C. The deviation at 10% H_2O is smaller compared to the deviation at 3% H_2O. This is an indication that the parasitic electronic leakage decreases at higher steam partial pressures.

Often, in literature, the ionic transport number eqn (10) is used to determine the contribution of ionic and electronic conductivity in electrolyte materials. In pure ionic conductors, the value for the electronic resistance is infinite and the ionic transport number is equal to 1. In contrast, the ionic transport number for a mixed ionic electronic conductor is between 0 and 1.

In Fig. 8(c) the ionic transport number of the BCZYYb7111 electrolyte is plotted as a function of temperature. At 10% H_2O, the ionic transport number decreases from 0.99 at 600 °C to 0.97 at 700 °C. The relatively high values for t_i indicate a large contribution from ionic conductivity and that BCZYYb7111 is nearly a pure ionic conductor under these conditions. Other electrolyte materials, such as BCZYYb4411, only reach ionic transport numbers of 0.95 at 600 °C.[18] This shows that BCZYYb7111 is a good electrolyte material for PCCs and exhibits low electronic leakage. In addition to temperature dependency, Fig. 8(c) also shows the steam partial pressure dependency of the ionic transport number. At 650 °C the ionic transport number increases from 0.91 to 0.97 by changing from dry conditions to 3% H_2O at the oxygen electrode. However, by further increasing the steam partial pressure, the ionic transport number increases only slightly to 0.98 at 10% H_2O. A further increase in steam partial pressures has nearly no impact on the ionic transport number. This indicates that the ionic conductivity was almost saturated at 10% H_2O. Our results clearly show that parasitic electronic leakage in PCECs can be mitigated by using temperatures below 600 °C and steam partial pressures above 10% H_2O.

The faradaic efficiency was determined by calculating the protonic current in the electrolyte and dividing it by the measured current in the outer circuit according to:

$$FE = \frac{I_{H^+}}{I_{meas}} \quad (13)$$

where I_{H^+} is the protonic current in the electrolyte and I_{meas} is the measured electronic current in the outer circuit. The protonic current along the ionic railway and the measured electronic current can be expressed as:

$$I_{H^+} = \frac{V_{Cell} - V_N}{R_i + R_{p,r}} \quad (14)$$

$$I_{meas} = \frac{V_{Cell} - V_{OCV}}{R_{DC}} \quad (15)$$

where V_{cell} is the applied cell voltage. In eqn (14) and (15) a linear behavior between cell voltage and current is assumed. This is not totally correct, especially in the low current density region where activation losses for the reaction at the electrodes dominate.[18] However, considering the constant slopes in the *iV* curves (Fig. 3), linear behavior is a valid assumption. Furthermore, the expressions provide a valuable estimate to calculate the faradaic efficiencies.

Fig. 8(d) shows the calculated faradaic efficiency in dependence of the current density. The faradaic efficiency increases with increasing current density. For instance, at 600 °C and an electrolysis current density of −60 mA cm^{-2}, a faradaic efficiency of 90.4%, 93.8% and 92.3% were achieved at 3, 10 and 20% steam partial pressures, respectively. These are among the highest values ever reported. In other studies faradaic efficiencies of only ~50% were reported for a BGLC/BZCY/Ni-BZCY cell configuration at 600 °C, 1.5 bar steam and – 100 mA cm^{-2} electrolysis current density.[31] One reason for the comparably high faradaic efficiency in our electrolyte supported cell could be that the relatively thick electrolyte mitigates the influence of anodic overpotentials on the formation of electron holes in the electrolyte.[10] With an increasing distance from the anodic overpotentials at the oxygen electrode, lower concentrations of electron holes are obtained.[10,25] Thus, increasing the electrolyte thickness could decrease p-type conductivity in the electrolyte and mitigate parasitic electronic leakage. In contrast, decreasing the electrolyte thickness leads to decreased ohmic losses. This trade-off clearly shows that optimizing the electrolyte thickness is important to obtain high current densities and high faradaic efficiencies simultaneously.

At 700 °C and −130 mA cm^{-2} electrolysis current density, faradaic efficiencies of 84.3%, 88.8% and 90.7% were achieved

© 2024 The Author(s). Published by the Royal Society of Chemistry

Open Access Article. Published on 04 March 2024. Downloaded on 2/23/2026 10:43:05 PM.
This article is licensed under a Creative Commons Attribution 3.0 Unported Licence.

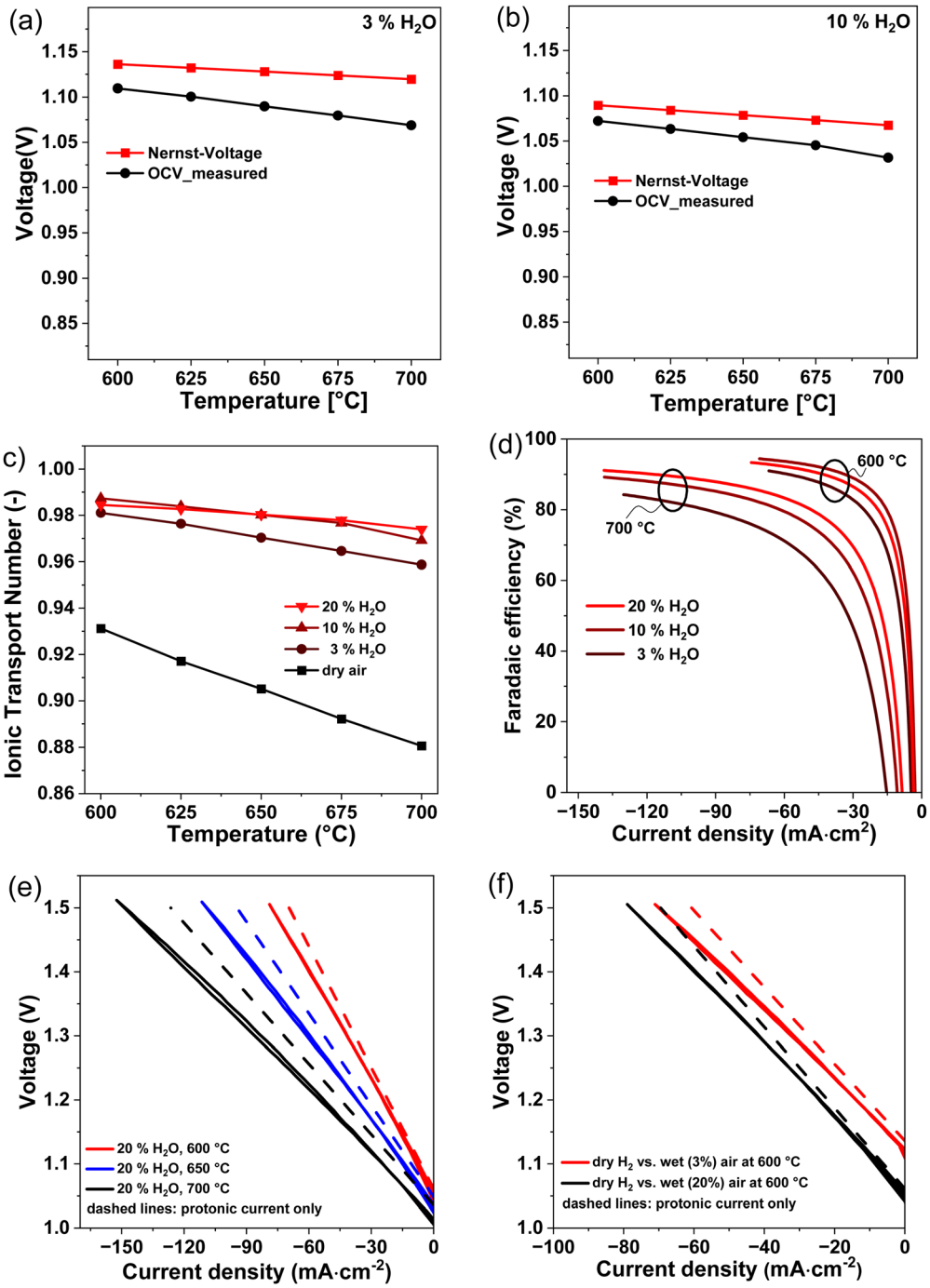

Fig. 8 Measured open circuit voltages (V_{OCV}) and theoretical Nernst voltages (V_N) as a function of temperature at (a) 3% H_2O (b) 10% H_2O at the oxygen electrode. (c) Ionic transport numbers as a function of temperature. (d) Calculated faradaic efficiency as a function of current density. (e) and (f) *iV* curve in electrolysis mode with calculated protonic current only. Wet air (0–20% H_2O) was used at the oxygen electrode and dry hydrogen at the fuel electrode.

at 3, 10 and 20% steam partial pressures, respectively. It is evident that the faradaic efficiency increases with decreasing temperatures and increasing steam partial pressures.

In electrolysis cells with a faradaic efficiency lower than 100%, the *iV* curves have to be corrected, considering that not all electrons measured in the outer circuit contribute to the hydrogen evolution reaction. The protonic current (I_{H^+}) that contributes to the HER is smaller than the measured current (I_{meas}) in the outer circuit. Fig. 8(e) and (f) show the measured *iV* curves in electrolysis mode and the corrected *iV* curves with the protonic current only. The deviation between protonic current (I_{H^+}) contributing to the HER and measured electronic current (I_{meas}) determines the electronic leakage ($I_e = I_{meas} - I_{H^+}$). At a fixed steam partial pressure of 20% H_2O and at 1.3 V the electronic leakage decreases from 14.6 mA cm^{-2} to 7.7 mA cm^{-2} to 5.7 mA cm^{-2} by lowering the temperature from 700 °C

Open Access Article. Published on 04 March 2024. Downloaded on 2/23/2026 10:43:05 PM.
This article is licensed under a Creative Commons Attribution 3.0 Unported Licence.

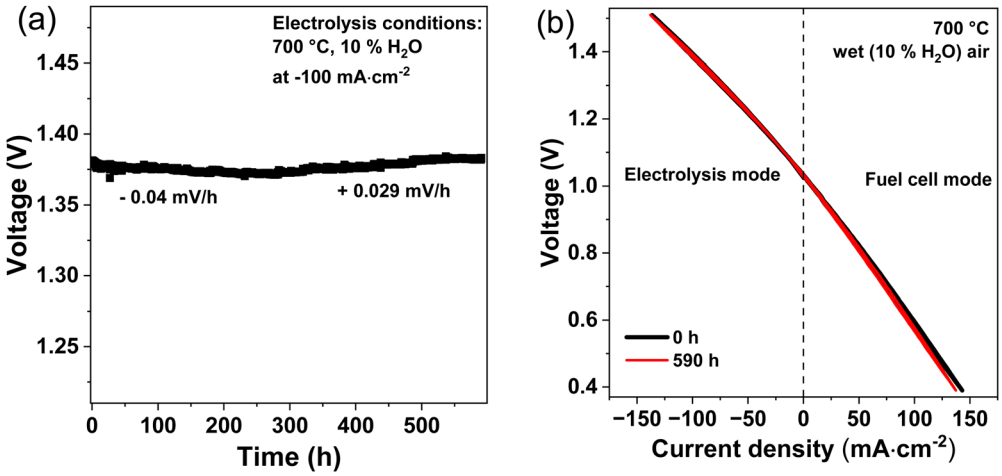

Fig. 9 (a) Cell voltage over time during degradation test of the electrolyte supported PNO/BCZYYb/Ni-BZY cell at the electrolysis current density of −100 mA cm^{-2}. (b) *iV* curves before and after 590 h in electrolysis operation. The temperature was set to 700 °C. Wet air (10% H_2O) was used at the oxygen electrode and dry hydrogen at the fuel electrode.

to 650 °C to 600 °C (Fig. 8(e)). This indicates smaller parasitic electronic leakage at lower temperatures. At a fixed temperature of 600 °C and at 1.3 V the electronic leakage decreases from 4.5 mA cm^{-2} to 4.1 mA cm^{-2} by increasing the steam partial pressure from 3% to 20% H_2O. This indicates smaller parasitic electronic leakage at higher steam partial pressures.

3.2.5. Long-term durability in electrolysis mode. To investigate the long-term durability of the PNO/BCZYYb/Ni-BZY electrolyte supported single cells, the cells were operated in electrolysis mode for 590 h. It is noteworthy to mention that long-term measurements in electrolysis mode are scare and only a few studies report on long-term measurements over 500 h.[10,18,29] Furthermore, in most studies steam partial pressures below 30% H_2O are used.[10,18,29] At higher steam partial pressures barium cerate zirconates tend to decompose and form barium carbonates or barium hydroxides.[14–17] To compare our results with literature, wet air (10% H_2O) was used at the oxygen electrode and dry hydrogen at the fuel electrode, respectively. The temperature was set to 700 °C. An electrolysis current density of −100 mA cm^{-2} was applied and the cell voltage was measured over time. Fig. 9(a) shows the measured voltage over time. During the first 250 h, the voltage slightly decreased from 1.38 V to 1.37 V and then increased again to 1.38 V at 590 h, giving a degradation rate of 0.029 mV h^{-1} over the last 340 h. This shows a very stable operation in electrolysis mode and a high durability of the single cells. The voltage drop during the first 250 h can be attributed to improving contact resistances during operation. Other studies reported a similar degradation rate of 0.03 mV h^{-1} for a BCFZY/BCZYYb/Ni-BCZYYb single cell operated at an electrolysis current density of 1385 mA cm^{-2} in wet air (20% H_2O) at the oxygen electrode and at 600 °C.[10]

After 590 h of operation, an *iV* curve was recorded again and compared with the curve recorded at the start of the degradation test. Fig. 9(b) shows the *iV* curves before and after the degradation test, whereby remarkably nearly no difference is observed.

3.2.6. Post-test characterization. After long-term measurements in electrolysis mode, the cells were characterized by SEM to identify any deterioration in the electrolyte and electrodes.

No structural deterioration of the cell layers or delamination of the electrodes from the electrolyte is observed (Fig. 10). The electrolyte still shows a dense structure, while both the fuel and oxygen electrode show sufficient porosity for gas transport. However, a very thin interfacial layer can be observed between the oxygen electrode and the electrolyte. This interfacial layer between PNO and proton ceramic electrolytes was already observed in other studies. It forms during sintering of PNO on BCZY electrolytes at high temperatures (>1150 °C).[43] However, the interfacial layer is not expected to have any detrimental effects on cell performance.[43]

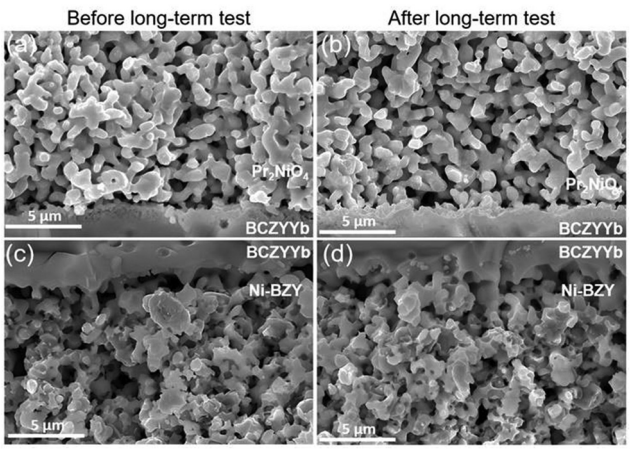

Fig. 10 SEM images of PNO/BCZYYb/Ni-BZY single cell after long-term measurement in electrolysis operation for 590 h, (a) and (b) oxygen electrode/electrolyte interface (c) and (d) fuel electrode/electrolyte interface.

4. Conclusion

In this study electrolyte supported proton ceramic electrolysis cells (PCECs) were successfully fabricated *via* the solid state

© 2024 The Author(s). Published by the Royal Society of Chemistry

Open Access Article. Published on 04 March 2024. Downloaded on 2/23/2026 10:43:05 PM. This article is licensed under a Creative Commons Attribution 3.0 Unported Licence.

reactive sintering method. The ceria rich BCZYYb7111 electrolyte support showed high proton conductivity and low ohmic resistances related to the high electrolyte thickness of 850 μm. For example, BCZYYb7111 (5 mΩ cm^2 μm^{-1}) exhibits a 6 times lower specific ohmic resistance than BZCY541 (30 mΩ cm^2 μm^{-1}).[29] Moreover, high ionic transport numbers of 0.99 at 600 °C and 10% H_2O were achieved, indicating that the electrolyte is gas tight and is a nearly pure ionic conductor. At an electrolysis current density of −75 mA cm^{-2} a high faradaic efficiency of 94% was calculated at 600 °C and 10% H_2O. These faradaic efficiencies are among the highest ever reported. For comparison, electrode supported BGLC/BCZY/Ni-BCZY single cells only reach faradaic efficiencies of ∼50% at 600 °C, 1.5 bar steam and −100 mA cm^{-2}.[31]

The comparison of $Pr_2NiO_{4+\delta}$ (PNO) and $Ba_{0.5}Sr_{0.5}Co_{0.8}Fe_{0.2}O_{3-\delta}$ (BSCF) as oxygen electrode showed higher performance for PNO in both electrolysis and fuel cell mode. At 600 °C, the polarization resistance (R_p) increased from 1.25 Ω cm^2 for a cell with PNO as oxygen electrode to 2.61 Ω cm^2 for a cell with BSCF as oxygen electrode. Long-term measurements of PNO/BCZYYb7111/Ni-BZY91 single cells in electrolysis mode up to 590 h showed stable operation with a small degradation rate of 0.029 mV h^{-1} over the last 340 h. Post-test characterization using SEM showed no deterioration in the electrode, electrolyte and electrode/electrolyte interface.

Conflicts of interest

There are no conflicts to declare.

Acknowledgements

The Helmholtz Association of German Research Centers (HGF) and the Federal Ministry of Education and Research (BMBF), Germany are gratefully acknowledged for their support within the frame of the Innovation Pool project ''Solar H2: Highly Pure and Compressed'' and the Helmholtz Research Program ''Materials and Technologies for the Energy Transition'' (MTET).

References

1 E. Fabbri, L. Bi, D. Pergolesi and E. Traversa, Towards the Next Generation of Solid Oxide Fuel Cells Operating Below 600 °C with Chemically Stable Proton-Conducting Electrolytes, *Adv. Mater.*, 2012, **24**, 195–208.
2 Q. Wang, S. Ricote and M. Chen, Oxygen electrodes for protonic ceramic cells, *Electrochim. Acta*, 2023, **446**, 142101.
3 L. Bi, S. Boulfrad and E. Traversa, Steam electrolysis by solid oxide electrolysis cells (SOECs) with proton-conducting oxides, *Chem. Soc. Rev.*, 2014, **43**, 8255–8270.
4 E. Fabbri, D. Pergolesi and E. Traversa, Materials challenges toward proton-conducting oxide fuel cells: a critical review, *Chem. Soc. Rev.*, 2010, **39**, 4355–4369.
5 W. Zhang and Y. H. Hu, Progress in proton-conducting oxides as electrolytes for low-temperature solid oxide fuel cells: From materials to devices, *Energy Sci. Eng.*, 2021, **9**, 984–1011.
6 K. D. Kreuer, Proton-Conducting Oxides, *Annu. Rev. Mater. Res.*, 2003, **33**, 333–359.
7 L. Yang, S. Wang, K. Blinn, M. Liu, Z. Liu, Z. Cheng and M. Liu, Enhanced sulfur and coking tolerance of a mixed ion conductor for SOFCs: $BaZr_{0.1}Ce_{0.7}Y_{0.2-x}Yb_xO_{3-\delta}$, *Science*, 2009, **326**, 126–129.
8 N. A. Danilov, I. A. Starostina, G. N. Starostin, A. V. Kasyanova, D. A. Medvedev and Z. Shao, Fundamental Understanding and Applications of Protonic Y- and Yb-Coped $Ba(Ce,Zr)O_3$ Perovskites: State-of-the-Art and Perspectives, *Adv. Energy Mater.*, 2023, **13**(47), 2302175.
9 H. Su and Y. H. Hu, Degradation issues and stabilization strategies of protonic ceramic electrolysis cells for steam electrolysis, *Energy Sci. Eng.*, 2022, **10**, 1706–1725.
10 C. Duan, R. Kee, H. Zhu, N. Sullivan, L. Zhu, L. Bian, D. Jennings and R. O'Hayre, Highly efficient reversible protonic ceramic electrochemical cells for power generation and fuel production, *Nat. Energy*, 2019, **4**, 230–240.
11 C. Duan, J. Huang, N. Sullivan and R. O'Hayre, Proton-conducting oxides for energy conversion and storage, *Appl. Phys. Rev.*, 2020, **7**, 11314.
12 M. Liang, Y. Wang, Y. Song, D. Guan, J. Wu, P. Chen, A. Maradesa, M. Xu, G. Yang, W. Zhou, W. Wang, R. Ran, F. Ciucci and Z. Shao, High-temperature water oxidation activity of a perovskite-based nanocomposite towards application as air electrode in reversible protonic ceramic cells, *Appl. Catal., B*, 2023, **331**, 122682.
13 W. Li, B. Guan, T. Yang, Z. Li, W. Shi, H. Tian, L. Ma, T. L. Kalapos and X. Liu, Layer-structured triple-conducting electrocatalyst for water-splitting in protonic ceramic electrolysis cells: Conductivities vs. activity, *J. Power Sources*, 2021, **495**, 229764.
14 A. VahidMohammadi and Z. Cheng, Fundamentals of Synthesis, Sintering Issues, and Chemical Stability of $BaZr_{0.1}Ce_{0.7}Y_{0.1}Yb_{0.1}O_{3-\delta}$ Proton Conducting Electrolyte for SOFCs, *J. Electrochem. Soc.*, 2015, **162**, F803–F811.
15 S. Choi, C. J. Kucharczyk, Y. Liang, X. Zhang, I. Takeuchi, H.-I. Ji and S. M. Haile, Exceptional power density and stability at intermediate temperatures in protonic ceramic fuel cells, *Nat. Energy*, 2018, **3**, 202–210.
16 Y. Zhang, D. Xie, B. Chi, J. Pu, J. Li and D. Yan, Basic properties of proton conductor $BaZr_{0.1}Ce_{0.7}Y_{0.1}Yb_{0.1}O_{3-\delta}$ (BZCYYb) material, *Asia-Pac. J. Chem. Eng.*, 2019, **14**(4), e2322.
17 D. A. Medvedev, J. G. Lyagaeva, E. V. Gorbova, A. K. Demin and P. Tsiakaras, Advanced materials for SOFC application: Strategies for the development of highly conductive and stable solid oxide proton electrolytes, *Prog. Mater. Sci.*, 2016, **75**, 38–79.
18 S. Choi, T. C. Davenport and S. M. Haile, Protonic ceramic electrochemical cells for hydrogen production and electricity generation: exceptional reversibility, stability, and demonstrated faradaic efficiency, *Energy Environ. Sci.*, 2019, **12**, 206–215.

Open Access Article. Published on 04 March 2024. Downloaded on 2/23/2026 10:43:05 PM. This article is licensed under a Creative Commons Attribution 3.0 Unported Licence.

19 F. Liu, H. Deng, D. Diercks, P. Kumar, M. H. A. Jabbar, C. Gumeci, Y. Furuya, N. Dale, T. Oku, M. Usuda, P. Kazempoor, L. Fang, D. Chen, B. Liu and C. Duans, Lowering the operating temperature of protonic ceramic electrochemical cells to <450 °C, *Nat. Energy*, 2023, **8**, 1145–1157.

20 H. Ding, W. Wu, C. Jiang, Y. Ding, W. Bian, B. Hu, P. Singh, C. J. Orme, L. Wang, Y. Zhang and D. Ding, Self-sustainable protonic ceramic electrochemical cells using a triple conducting electrode for hydrogen and power production, *Nat. Commun.*, 2020, **11**, 1907.

21 I.-H. Kim, D.-K. Lim, Y. Namgung, H. Bae, J.-Y. Park and S.-J. Song, Electrical properties of $BaZr_{0.5}Ce_{0.3}Y_{0.1}Yb_{0.1}O_{3-\delta}$ proton conductor for reversible proton-conducting solid oxide electrochemical cells, *Acta Mater.*, 2023, **249**, 118800.

22 H.-T. Lim, A. K. Niaz, T. Prasankumar, M. J. Kim, S. Kang, J.-Y. Park and A. V. Virkar, Understanding Chemo-Mechanical Stability of Protonic Ceramic Cells Through Electronic Conduction in the $BaCe_{0.7}Zr_{0.1}Y_{0.1}Yb_{0.1}O_{3-\delta}$ Electrolyte, *J. Electrochem. Soc.*, 2023, **170**, 34503.

23 A. K. Niaz, Y. J. Kim, A. V. Virkar, J.-Y. Park and H.-T. Lim, Design concept of co-ionic conducting solid oxide electrolyte for stable operation in a cell-imbalanced fuel cell stack, *J. Power Sources*, 2021, **512**, 230483.

24 I. Zvonareva, X.-Z. Fu, D. Medvedev and Z. Shao, Electrochemistry and energy conversion features of protonic ceramic cells with mixed ionic-electronic electrolytes, *Energy Environ. Sci.*, 2022, **15**, 439–465.

25 H. Zhu, S. Ricote and R. J. Kee, Faradaic efficiency in protonic-ceramic electrolysis cells, *J. Phys. Energy*, 2022, **4**, 14002.

26 H. Zhu, S. Ricote, C. Duan, R. P. O'Hayre, D. S. Tsvetkov and R. J. Kee, Defect Incorporation and Transport within Dense $BaZr_{0.8}Y_{0.2}O_{3-\delta}$ (BZY20) Proton-Conducting Membranes, *J. Electrochem. Soc.*, 2018, **165**, F581–F588.

27 P. S. Gaikwad, K. Mondal, Y. K. Shin, A. C. T. van Duin and G. Pawar, Enhancing the faradaic efficiency of solid oxide electrolysis cells: progress and perspective, *npj Comput. Mater.*, 2023, **9**, DOI: 10.1038/s41524-023-01044-1.

28 X. Jin and Y. Shoukry, Current Leakage and faradaic Efficiency Simulation of Proton-Conducting Solid Oxide Electrolysis Cells, *ECS Trans.*, 2023, **111**, 1159–1167.

29 H. Zheng, M. Riegraf, N. Sata and R. Costa, A double perovskite oxygen electrode in Zr-rich proton conducting ceramic cells for efficient electricity generation and hydrogen production, *J. Mater. Chem. A*, 2023, **11**, 10955–10970.

30 L. Zhu, R. O'Hayre and N. P. Sullivan, High performance tubular protonic ceramic fuel cells via highly-scalable extrusion process, *Int. J. Hydrogen Energy*, 2021, **46**, 27784–27792.

31 E. Vøllestad, R. Strandbakke, M. Tarach, D. Catalán-Martínez, M.-L. Fontaine, D. Beeaff, D. R. Clark, J. M. Serra and T. Norby, Mixed proton and electron conducting double perovskite anodes for stable and efficient tubular proton ceramic electrolysers, *Nat. Mater.*, 2019, **18**, 752–759.

32 Y. Okuyama, Y. Harada, Y. Mikami, K. Yamauchi, T. Kuroha, H. Shimada, Y. Yamaguchi and Y. Mizutani, Evaluation of Hydrogen Ions Flowing through Protonic Ceramic Fuel Cell Using Ytterbium-Doped Barium Zirconate as Electrolyte, *J. Electrochem. Soc.*, 2023, **170**, 84509.

33 M. Papac, V. Stevanović, A. Zakutayev and R. O'Hayre, Triple ionic-electronic conducting oxides for next-generation electrochemical devices, *Nat. Mater.*, 2021, **20**, 301–313.

34 H. An, H.-W. Lee, B.-K. Kim, J.-W. Son, K. J. Yoon, H. Kim, D. Shin, H.-I. Ji and J.-H. Lee, A 5×5 cm^2 protonic ceramic fuel cell with a power density of 1.3 W cm^{-2} at 600 °C, *Nat. Energy*, 2018, **3**, 870–875.

35 A. K. Azad, A. M. Abdalla, A. Afif, A. Azad, S. Afroze, A. C. Idris, J.-Y. Park, M. Saqib, N. Radenahmad, S. Hossain, I. B. Elius, M. Al-Mamun, J. Zaini, A. Al-Hinai, M. S. Reza and J. T. S. Irvine, Improved mechanical strength, proton conductivity and power density in an 'all-protonic' ceramic fuel cell at intermediate temperature, *Sci. Rep.*, 2021, **11**, 19382.

36 C. Duan, D. Hook, Y. Chen, J. Tong and R. O'Hayre, Zr and Y co-doped perovskite as a stable, high performance cathode for solid oxide fuel cells operating below 500 °C, *Energy Environ. Sci.*, 2017, **10**, 176–182.

37 S. Rajendran, N. K. Thangavel, H. Ding, Y. Ding, D. Ding and L. M. Reddy Arava, Tri-Doped $BaCeO_3$-$BaZrO_3$ as a Chemically Stable Electrolyte with High Proton-Conductivity for Intermediate Temperature Solid Oxide Electrolysis Cells (SOECs), *ACS Appl. Mater. Interfaces*, 2020, **12**, 38275–38284.

38 S. Choi, S. Yoo, J. Kim, S. Park, A. Jun, S. Sengodan, J. Kim, J. Shin, H. Y. Jeong, Y. Choi, G. Kim and M. Liu, Highly efficient and robust cathode materials for low-temperature solid oxide fuel cells: $PrBa_{0.5}Sr_{0.5}Co_{2-x}Fe_xO_{5+\delta}$, *Sci. Rep.*, 2013, **3**, 2426.

39 W. Li, B. Guan, L. Ma, S. Hu, N. Zhang and X. Liu, High performing triple-conductive $Pr_2NiO_{4+\delta}$ anode for proton-conducting steam solid oxide electrolysis cell, *J. Mater. Chem. A*, 2018, **6**, 18057–18066.

40 A. Grimaud, F. Mauvy, J. M. Bassat, S. Fourcade, L. Rocheron, M. Marrony and J. C. Grenier, Hydration Properties and Rate Determining Steps of the Oxygen Reduction Reaction of Perovskite-Related Oxides as H + –SOFC Cathodes, *J. Electrochem. Soc.*, 2012, **159**, B683–B694.

41 H. Tian, W. Li, L. Ma, T. Yang, B. Guan, W. Shi, T. L. Kalapos and X. Liu, Deconvolution of Water-Splitting on the Triple-Conducting Ruddlesden-Popper-Phase Anode for Protonic Ceramic Electrolysis Cells, *ACS Appl. Mater. Interfaces*, 2020, **12**, 49574–49585.

42 J. Cao, Y. Ji and Z. Shao, Perovskites for protonic ceramic fuel cells: a review, *Energy Environ. Sci.*, 2022, **15**, 2200–2232.

43 J. Dailly, F. Mauvy, M. Marrony, M. Pouchard and J.-C. Grenier, Electrochemical properties of perovskite and A2MO4-type oxides used as cathodes in protonic ceramic half cells, *J. Solid State Electrochem.*, 2011, **15**, 245–251.

44 V. Vibhu, I. C. Vinke, R.-A. Eichel and L. de Haart, Cobalt substituted $Pr_2Ni_{1-x}Co_xO_{4+\delta}$ (x = 0, 0.1, 0.2) oxygen electrodes: Impact on electrochemical performance and durability of solid oxide electrolysis cells, *J. Power Sources*, 2021, **482**, 228909.

© 2024 The Author(s). Published by the Royal Society of Chemistry

Open Access Article. Published on 04 March 2024. Downloaded on 2/23/2026 10:43:05 PM.
This article is licensed under a Creative Commons Attribution 3.0 Unported Licence.

45 I. D. Unachukwu, V. Vibhu, I. C. Vinke, R.-A. Eichel and L. de Haart, Electrochemical and degradation behaviour of single cells comprising Ni-GDC fuel electrode under high temperature steam- and co-electrolysis conditions, *J. Power Sources*, 2023, **556**, 232436.

46 V. Vibhu, I. C. Vinke, F. Zaravelis, S. G. Neophytides, D. K. Niakolas, R.-A. Eichel and L. G. J. de Haart, Performance and Degradation of Electrolyte-Supported Single Cell Composed of Mo–Au–Ni/GDC Fuel Electrode and LSCF Oxygen Electrode during High Temperature Steam Electrolysis, *Energies*, 2022, **15**, 2726.

47 M. C. Tucker, L. Cheng and L. C. DeJonghe, Selection of cathode contact materials for solid oxide fuel cells, *J. Power Sources*, 2011, **196**, 8313–8322.

48 S. Foit, L. Dittrich, T. Duyster, I. Vinke, R.-A. Eichel and L. G. J. de Haart, Direct Solid Oxide Electrolysis of Carbon Dioxide: Analysis of Performance and Processes, *Processes*, 2020, **8**, 1390.

49 P. A. Stuart, T. Unno, J. A. Kilner and S. J. Skinner, Solid oxide proton conducting steam electrolysers, *Solid State Ionics*, 2008, **179**, 1120–1124.

50 N. Bausá, S. Escolástico and J. M. Serra, Direct CO_2 conversion to syngas in a $BaCe_{0.2}Zr_{0.7}Y_{0.1}O_{3-\delta}$-based proton-conducting electrolysis cell, *J. CO2 Util.*, 2019, **34**, 231–238.

51 R. Merkle, M. F. Hoedl, G. Raimondi, R. Zohourian and J. Maier, Oxides with Mixed Protonic and Electronic Conductivity, *Annu. Rev. Mater. Res.*, 2021, **51**, 461–493.

© 2024 The Author(s). Published by the Royal Society of Chemistry